scientific reports

Check for updates

OPEN

SETD8 promotes ovarian clear cell carcinoma by epigenetically activating RNA metabolism genes via H4K20me1

Eri Suzuki-Ariyoshi[1,5], Syuzo Kaneko[2,3,5]✉, Kenbun Sone[1]✉, Noriko Ikawa[2], Ryuta Hachijo[1], Yuri Jonouchi[1], Natsumi Tsuboyama[1], Ayumi Taguchi[1], Ken Asada[2,3], Masaaki Komatsu[2,3], Takayuki Iriyama[1], Katsutoshi Oda[4], Yutaka Osuga[1], Yasushi Hirota[1] & Ryuji Hamamoto[2,3]

Ovarian clear cell carcinoma (OCCC) is a chemoresistant subtype of epithelial ovarian cancer with limited therapeutic options and distinct molecular features. Histone methyltransferase SETD8 catalyzes the monomethylation of histone H4 at lysine 20 (H4K20me1) and has been implicated in transcriptional regulation across multiple cancer types. In endometrial cancer, we previously demonstrated that SETD8 regulates downstream targets through integrative ChIP-seq and RNA-seq analyses, linking its activity to p53-dependent signaling pathways. However, the role of SETD8 in OCCC and its potential tumor-context–specific functions remain undefined. Integrative analyses of ChIP-seq and RNA-seq in OCCC revealed that SETD8 maintains the expression of genes critical for RNA processing, including *HNRNPA2B1*, *EIF4G1*, and *SRSF3*, in a manner independent of p53 signaling. Pharmacological inhibition or RNA interference–mediated depletion of SETD8 resulted in a pronounced reduction of global H4K20me1 levels, impaired cellular proliferation, and increased lipid peroxidation consistent with ferroptotic stress. Transcriptomic profiling further demonstrated that SETD8 inhibition reprograms ferroptosis-associated gene expression, establishing a mechanistic link between chromatin-based transcriptional control and cellular redox vulnerability. Furthermore, clinical data analysis from public datasets (GSE29450 and TCGA-KIRC) confirmed that SETD8 is significantly overexpressed in OCCC tissues compared to normal counterparts and that high *SETD8* expression correlates with poor overall survival in clear cell lineage tumors, underscoring its potential as a clinical biomarker. Our study provides an in vitro mechanistic framework in which SETD8 safeguards RNA metabolic integrity and mitigates ferroptotic stress through epigenetic regulation in OCCC. These results underscore the lineage-specific roles of SETD8 across gynecologic malignancies and identify SETD8 as a potential therapeutic vulnerability that warrants further in vivo investigation.

Keywords SETD8, H4K20me1, Ovarian clear cell carcinoma, Ferroptosis, RNA processing, Epigenetics, p53-independent signaling

Ovarian clear cell carcinoma (OCCC) is an aggressive histologic subtype of epithelial ovarian cancer characterized by intrinsic resistance to platinum-based chemotherapy and a high prevalence in East Asian populations[1–4]. Genetically, OCCC is distinct from high-grade serous carcinoma, frequently harboring *ARID1A* loss-of-function and *PIK3CA* activating mutations[5,6]. Despite these molecular insights, effective targeted therapies remain limited, necessitating the identification of novel therapeutic vulnerabilities[7,8].

Histone methyltransferase SETD8 (KMT5A) catalyzes the monomethylation of histone H4 at lysine 20 (H4K20me1), regulating DNA replication and the DNA damage response[9–11]. While SETD8 is overexpressed and associated with poor prognosis in various malignancies, its role in OCCC remains undefined[12,13]. We previously reported that SETD8 regulates p53-dependent signaling in endometrial cancer[14]. However, the

[1]Department of Obstetrics and Gynecology, Graduate School of Medicine, The University of Tokyo, Tokyo 113-8655, Japan. [2]Division of Medical AI Research and Development, National Cancer Center Research Institute, 5-1-1 Tsukiji, Chuo-ku, Tokyo 104-0045, Japan. [3]AI Medical Engineering Team, RIKEN Center for Advanced Intelligence Project, Tokyo 103-0027, Japan. [4]Division of Integrative Genomics, Graduate School of Medicine, The University of Tokyo, Tokyo 113-8655, Japan. [5]Eri Suzuki-Ariyoshi and Syuzo Kaneko contributed equally to this work. ✉email: sykaneko@ncc.go.jp; ksone5274@gmail.com

metabolic and epigenetic landscape of OCCC—which shares significant similarities with kidney renal clear cell carcinoma (KIRC)—suggests a potentially distinct, lineage-specific role for SETD8 in these clear cell tumors[15,16].

A critical feature of clear cell lineage cancers is their unique redox vulnerability[16]. OCCC cells exhibit a high dependency on antioxidant systems to survive the iron-rich, oxidative environment of their endometriosis-associated origins[6]. This reliance makes OCCC particularly susceptible to ferroptosis, an iron-dependent form of non-apoptotic cell death driven by lipid peroxidation[17,18]. Key regulators such as *GPX4* and *SLC7A11* serve as metabolic safeguards against ferroptotic stress[19–21].

In this study, we hypothesized that SETD8 acts as an upstream epigenetic rheostat that maintains OCCC cell viability by safeguarding RNA metabolic integrity and mitigating ferroptotic stress. Unlike its p53-repressing function in endometrial cancer, we found that SETD8 in OCCC primarily activates genes involved in RNA processing and antioxidant defense. Our results demonstrate that SETD8 inhibition collapses this protective axis, sensitizing OCCC cells to ferroptosis and providing a novel therapeutic strategy for this chemoresistant malignancy.

Results

Integrated profiling of SETD8 targets

To gain insight into how SETD8-mediated chromatin regulation differs between OCCC and endometrial cancer cells, we performed comparative analyses of H4K20me1 ChIP-seq between OCCC (ES2, OVTOKO, OVISE, and RMG-I) and endometrial cancer cells (HEC50B and HEC1B), as previously described[14]. These cell lines were selected based on their widespread use in the literature and their well-characterized molecular features that are representative of their respective tumor types. Notably, OCCC is a genetically heterogeneous tumor type, and the selected cell lines (ES2, OVTOKO, OVISE, and RMG-I) reflect this diversity through variations in ARID1A mutation status, TP53 status, and other molecular traits. Likewise, HEC50B and HEC1B are commonly used endometrial carcinoma cell lines that exhibit prototypical features of this cancer type[22–24]. Hierarchical clustering of H4K20me1 enrichment profiles showed a separation between OCCC and endometrial cancer cell lines, implying potential context-dependent differences in SETD8-mediated chromatin regulation (Fig. 1A). Strikingly, we found that SETD8 targets were consistently enriched for genes involved in RNA processing and post-transcriptional regulation specifically in OCCC cell lines (Fig. 1B). These enrichment patterns were maintained when each of the four OCCC cell lines was analyzed individually (Supplementary Fig. 1).

To further explore the functional consequences of SETD8-mediated chromatin modification in OCCC, we performed integrative transcriptomic and epigenomic analyses by conducting RNA sequencing (RNA-seq) following SETD8 knockdown using Dicer–substrate small-interfering RNAs (DsiRNAs) at a concentration of 1 nM. These DsiRNAs, which are Dicer–substrate duplex RNAs, are processed intracellularly to generate active siRNAs, a feature that has been reported to enhance gene silencing efficiency and specificity relative to conventional siRNAs[25,26]. Differential expression analysis identified a consensus set of 284 upregulated and 296 downregulated genes that were consistently regulated across the OCCC cell lines (see Supplementary Fig. 2 for Venn diagrams and Supplementary Table 1 for the complete gene lists). Interestingly, and in contrast to our previous findings in endometrial cancer cells[14], SETD8 depletion in OCCC predominantly resulted in downregulation of target gene expression (Supplementary Fig. 3). Notably, genes associated with the p53 signaling pathway were not enriched among the SETD8-regulated targets in any of the OCCC cell lines, irrespective of their TP53 mutational status. Instead, the genes that were significantly downregulated following SETD8 knockdown showed functional enrichment in RNA processing and post-transcriptional regulation pathways. These included key regulators of mRNA translation, splicing, and ribosome biogenesis, such as *HNRNPA2B1*, *RPL5*, *SRSF3*, *EIF4G1*, *FUS*, and *PPIA*[27–32](Fig. 2). Genome browser tracks of ChIP-seq profiles demonstrated prominent H4K20me1 enrichment across promoter and gene body regions of these loci, supporting their direct regulation by SETD8 (Fig. 3). Collectively, these results raise the possibility that SETD8 promotes OCCC cell proliferation through epigenetic enhancement of RNA metabolic pathways, thereby supporting the high biosynthetic and proliferative demands characteristic of OCCC cells.

SETD8 plays a critical role in sustaining OCCC cell viability

Next, to functionally validate the role of SETD8 in ovarian clear cell carcinoma (OCCC), we treated four OCCC cell lines (ES2, OVISE, OVTOKO, and RMG-I) with UNC0379, a selective SETD8 inhibitor that exhibits high specificity over at least 15 other histone methyltransferases[33–36]. These cell lines were selected to represent the genetic heterogeneity of OCCC, including differences in ARID1A mutation status and the presence of wild-type TP53[24]. Treatment with UNC0379 significantly reduced global H4K20me1 levels in all four cell lines, indicating that SETD8 is the predominant H4K20 monomethyltransferase in OCCC cells (Fig. 4A, B). This treatment also led to a marked decrease in cell viability and colony formation, suggesting that SETD8 activity is essential for OCCC cell survival and proliferation (Fig. 4C, D). To validate these findings through genetic perturbation, SETD8 knockdown was performed as described above. Consistent with the effects observed upon pharmacological inhibition, SETD8 knockdown using DsiRNAs resulted in a marked reduction in global H4K20me1 levels (Fig. 4E, F) and significantly impaired cell proliferation across all tested OCCC cell lines (Fig. 4G), further substantiating the crucial role of SETD8 in maintaining OCCC cell growth through H4K20 monomethylation. Among the three DsiRNA constructs targeting SETD8, DsiRNA #2 and #3 exhibited higher knockdown efficiency, which corresponded with the most pronounced reduction in cell viability, indicating a direct correlation between SETD8 silencing and OCCC cell survival.

SETD8 inhibition induces ferroptosis

The above findings prompted us to investigate the mechanism of cell death triggered by SETD8 inhibition in OCCC cells. Although classical apoptotic features, such as increased Annexin V/PI staining, were not prominent

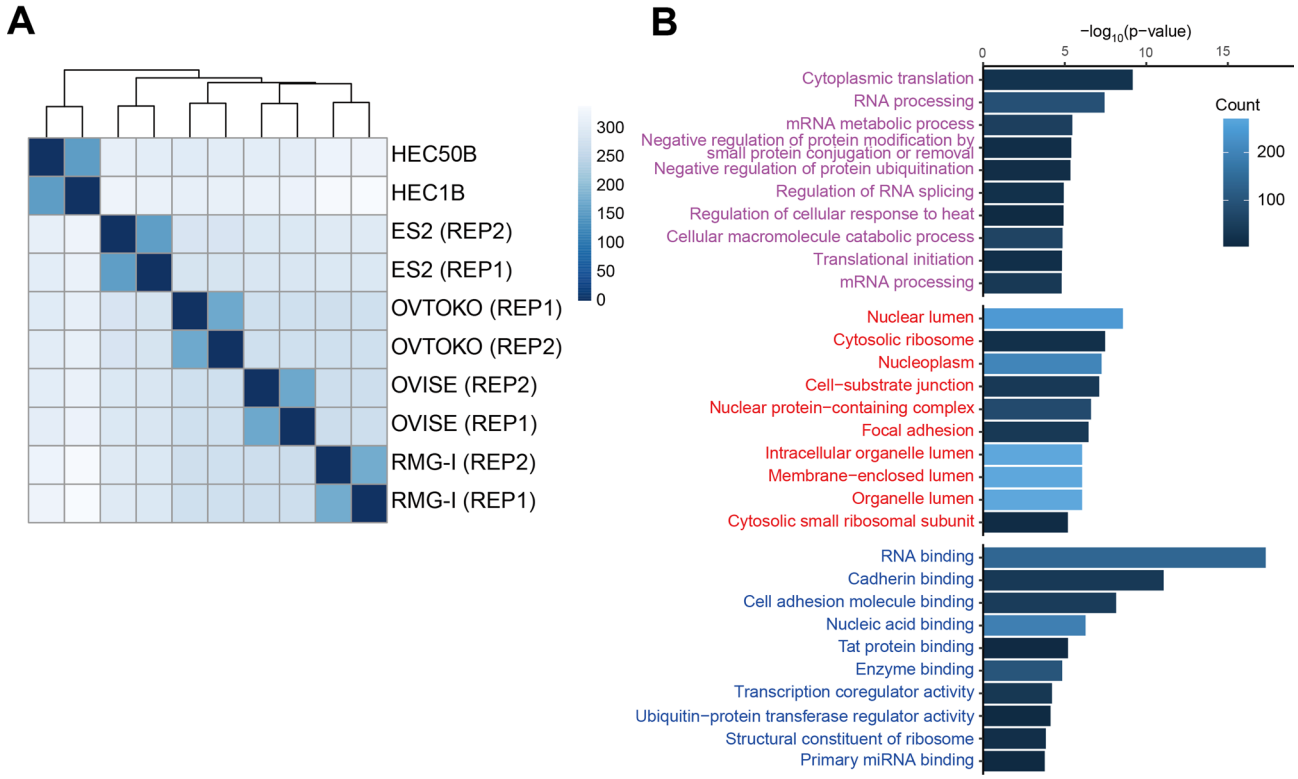

Fig. 1. H4K20me1-mediated chromatin regulation defines distinct epigenomic landscapes in OCCC. **A** Hierarchical clustering and sample-to-sample distance analysis of genome-wide H4K20me1 ChIP-seq profiles. OCCC cell lines (ES2, OVISE, OVTOKO, and RMG-I) and endometrial cancer cell lines (HEC50B and HEC1B) were analyzed based on variance-stabilizing transformed (VST) read counts across consensus peak regions. The heatmap displays Euclidean distances between samples; darker blue indicates higher global similarity (smaller distance), while lighter blue indicates lower similarity (larger distance). Samples are clustered into two distinct groups corresponding to their tumor types, highlighting tumor-type–specific H4K20me1 enrichment patterns. **B** Gene ontology (GO) enrichment analysis of H4K20me1 target genes identified in OCCC cell lines revealed that H4K20me1-enriched loci were significantly associated with genes involved in RNA processing and post-transcriptional regulation. GO terms are categorized by ontology: biological process (BP, purple), cellular component (CC, red), and molecular function (MF, blue), highlighting the functional relevance of SETD8 in RNA metabolic pathways in OCCC.

in our initial assays, we observed a significant increase in lipid peroxidation. This was indicated by enhanced lipid-ROS signals detected through C11-BODIPY staining (Supplementary Fig. 4A, B). These findings are indicative of ferroptosis, a regulated form of cell death characterized by the accumulation of lipid peroxides. Collectively, these results suggest that SETD8 inhibition induces ferroptotic cell death in OCCC cells. While ferroptosis vulnerability in OCCC has been previously reported[15], our findings newly identify SETD8 as an upstream epigenetic regulator of this susceptibility, providing a novel avenue for therapeutic exploitation.

Ferroptosis-related gene dysregulation

These findings suggest that SETD8 contributes to OCCC cell survival by maintaining redox homeostasis and that its depletion disrupts this balance, potentially leading to the induction of ferroptosis through the epigenetic dysregulation of metabolic pathways. To evaluate this possibility, we interrogated RNA-seq data generated from four OCCC cell lines subjected to SETD8 knockdown and quantified the expression of a ferroptosis-related gene panel, including *GPX4*, *SLC7A11*, *NCOA4*, *EPAS1*, *PTGS2*, *FTH1*, *FTL*, *TFRC*, *ACSL4*, *NFE2L2*, and *BACH1*[37,38] (Fig. 5A). Notably, quantitative RT–PCR validation confirmed increased expression of *EPAS1*, *ACSL4*, *NFE2L2*, and *BACH1*, which is consistent with the activation of a ferroptosis-related gene expression program in response to SETD8 inhibition[39](Fig. 5B). Among these genes, *NFE2L2*, which encodes the transcription factor NRF2, a master regulator of cellular antioxidant responses, exhibited H4K20me1 enrichment within its gene body across all four cell lines, suggesting that it may be a direct epigenetic target of SETD8 (Fig. 5C). In contrast, the expression changes observed in the other ferroptosis-related genes are more likely to reflect indirect regulatory effects or cell line–specific responses rather than direct transcriptional regulation by SETD8. Collectively, these findings indicate that SETD8 may contribute to ferroptosis resistance in OCCC by maintaining the expression of crucial antioxidant genes, such as GPX4 and SLC7A11, thereby promoting redox homeostasis and cellular adaptation during malignant transformation. Consequently, this establishes a lineage-specific metabolic vulnerability in OCCC and positions SETD8 as a therapeutic node for leveraging ferroptosis-based anticancer strategies.

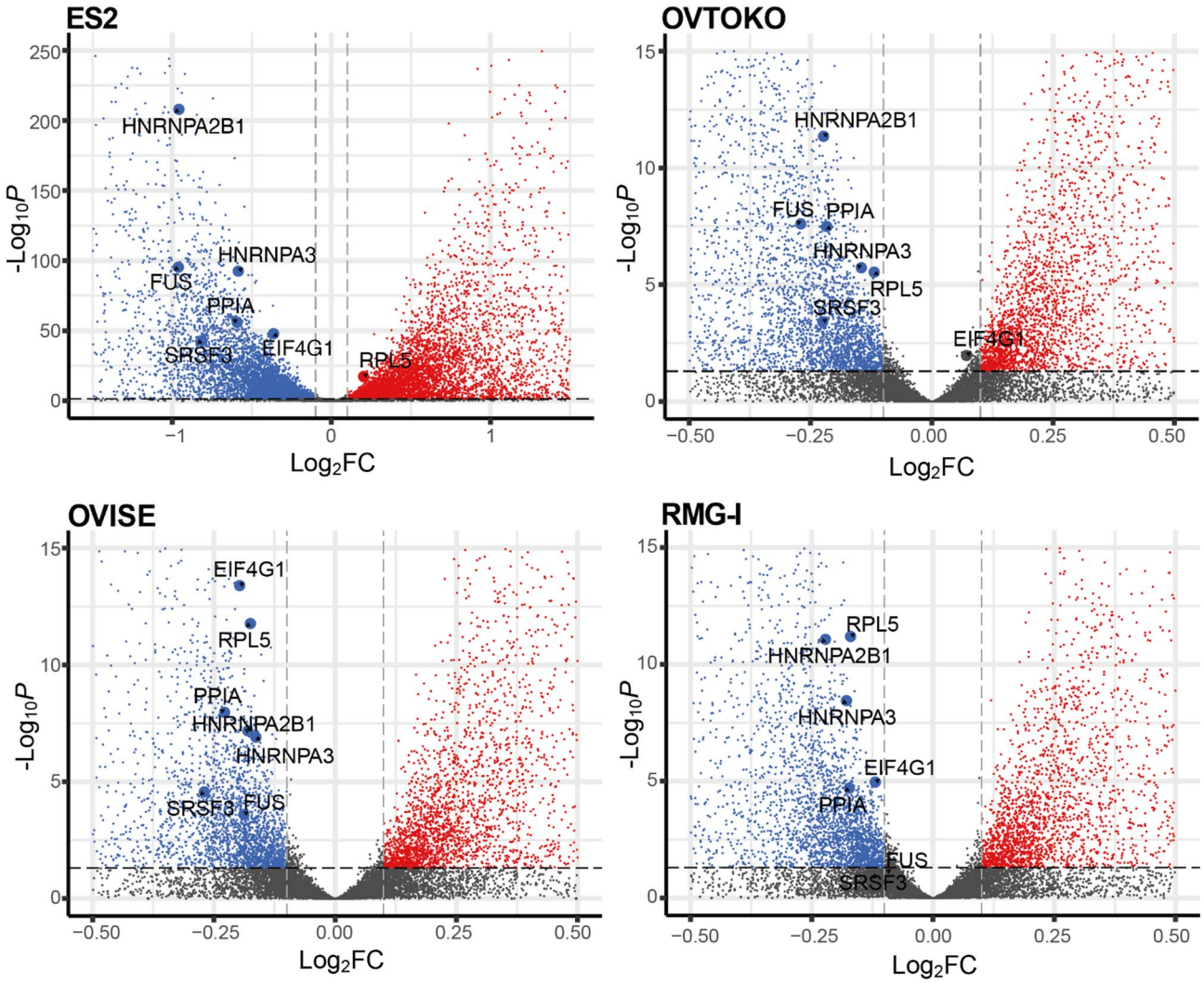

Fig. 2. SETD8 regulates RNA metabolic pathways independently of p53 signaling in OCCC. Volcano plots show transcriptomic changes following SETD8 knockdown in ES2, OVISE, OVTOKO, and RMG-I. Differentially expressed genes (DEGs) are highlighted in red (upregulated) and blue (downregulated), with larger dots indicating H4K20me1-bound DEGs based on ChIP-seq data. Representative SETD8 target genes involved in RNA metabolism are labeled.

Clinical significance of SETD8 in clear cell lineage tumors

To evaluate the clinical relevance of SETD8, we first compared its mRNA levels between OCCC and normal ovarian surface epithelium (OSE) using the GSE29450 dataset[40]. *SETD8* expression was significantly upregulated in OCCC tissues (Fig. 6A). While OCCC is a relatively rare subtype with limited clinical datasets, it shares striking histological and metabolic similarities with Kidney Renal Clear Cell Carcinoma (KIRC), which is characterized by the clear cell phenotype and a specific vulnerability to ferroptosis[15,16]. Given that SETD8 acts as an epigenetic regulator of the ferroptosis axis in our OCCC model, we utilized the large-scale TCGA-KIRC cohort ($n = 558$) as a representative clear-cell-lineage model to validate the clinical and prognostic impact of SETD8. The high statistical significance ($p = 0.00066$) observed in this cohort reinforces the role of SETD8 as a lineage-specific oncogenic driver across clear cell malignancies (Fig. 6B).

Discussion

In this study, we comprehensively investigated the functional role of SETD8 in OCCC and identified it as a critical regulator of chromatin dynamics, RNA metabolism, and ferroptosis resistance. Functional analyses revealed that pharmacological or genetic inhibition of SETD8 significantly impaired cell viability and clonogenicity across multiple OCCC cell lines, indicating that SETD8 activity is crucial for tumor cell survival. These effects were accompanied by a marked reduction in global H4K20me1 levels, confirming that SETD8 is the predominant enzyme responsible for this histone modification in OCCC. Notably, despite the presence of wild-type TP53 in these cell lines, SETD8 inhibition did not activate canonical p53 signaling, representing a major functional divergence from endometrial cancer, where SETD8 has been previously shown to induce p53-dependent

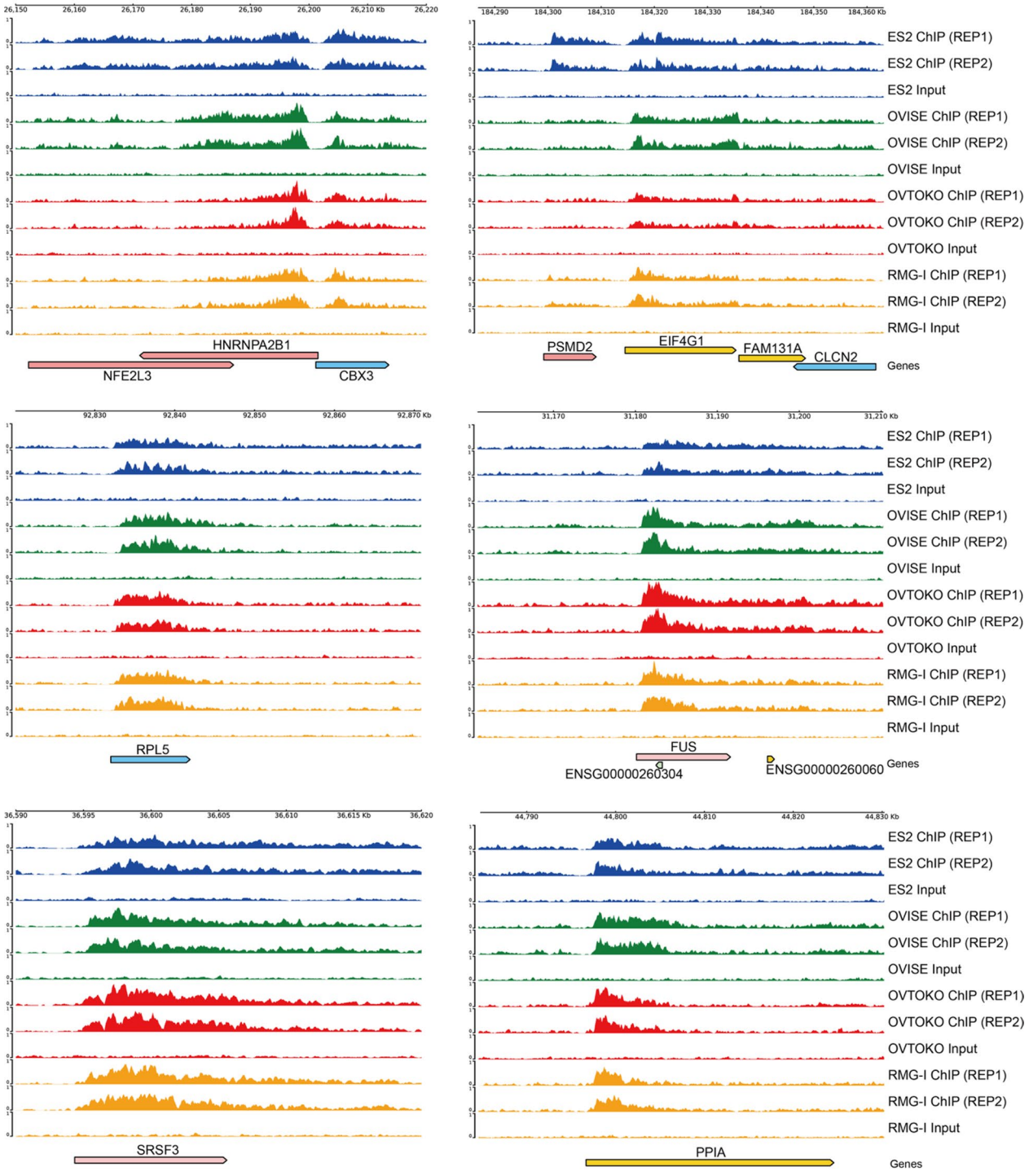

Fig. 3. Genome browser views of ChIP-seq profiles showing H4K20me1 enrichment at representative SETD8-regulated genes: *HNRNPA2B1*, *RPL5*, *SRSF3*, *EIF4G1*, *FUS and PPIA*.

apoptosis[14]. This observation underscores a novel, lineage-specific oncogenic role for SETD8 and suggests the existence of alternative, p53-independent survival pathways unique to the OCCC context.

Integrated ChIP-seq and RNA-seq analyses revealed that SETD8 regulates a subset of genes primarily involved in RNA processing, post-transcriptional regulation, and ribosome biogenesis. The consistent downregulation of these transcriptional programs following SETD8 depletion suggests that SETD8 is crucial for maintaining the transcriptional integrity of RNA metabolic pathways critical for the biosynthetic demands of rapidly proliferating OCCC cells. These findings are consistent with a recent study that demonstrated that SETD8 inhibition selectively targets cancer cells exhibiting heightened ribosome biogenesis activity[41]. Importantly, our results elucidate a previously unrecognized link between SETD8-mediated transcriptional maintenance of RNA metabolism

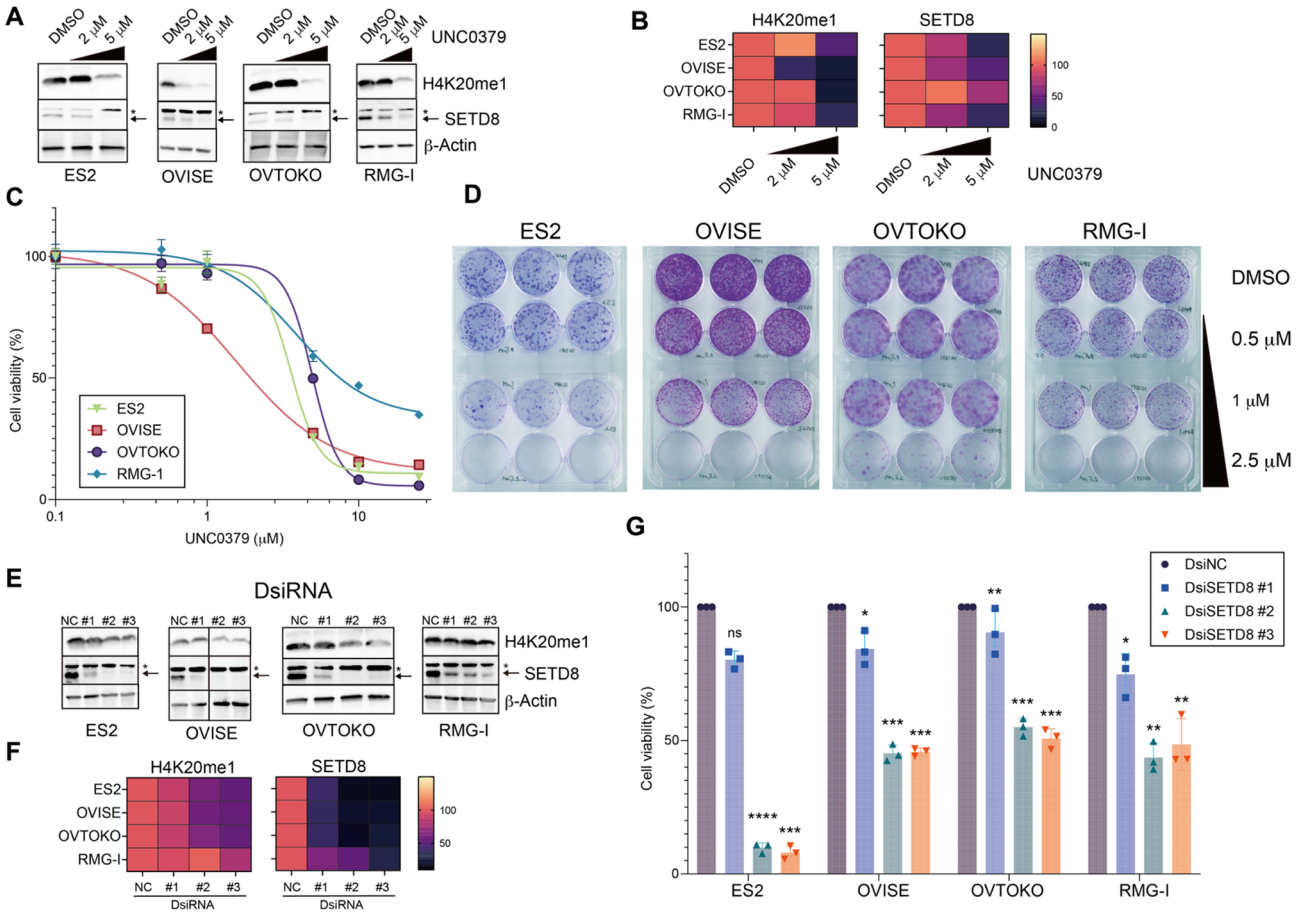

Fig. 4. SETD8 is essential for OCCC cell survival and proliferation. **A** Western blot analysis of H4K20me1 levels in four OCCC cell lines (ES2, OVISE, OVTOKO, RMG-I) following treatment with the SETD8 inhibitor UNC0379 (DMSO, 2, and 5 μM for 48 h). β-Actin was used as a loading control. The arrow indicates the band corresponding to SETD8. Asterisks (*) denote non-specific bands. **B** Quantification of H4K20me1 and SETD8 band intensities in each cell line shown in panel **A**. **C** Cell viability of the four OCCC cell lines after treatment with increasing concentrations (0.1–10 μM) of UNC0379 for 72 h, measured using the Cell Counting Kit-8. **D** Colony formation assays following treatment with UNC0379 (DMSO, 0.5, 1, and 2.5 μM) are shown, with representative images taken after 10–14 days of culture ($n = 3$). **E** Western blot analysis of H4K20me1 levels following SETD8 knockdown by three independent DsiRNAs (#1–3, 1 nM for 72 h). The western blots were conducted under the same experimental conditions, with the marker lane trimmed from the blot. See Supplementary Raw Data 1 for full images. **F** Quantification of H4K20me1 and SETD8 signal intensities in each cell line following DsiRNA treatment, as shown in panel **E**. **G** Cell viability of OCCC cell lines following transfection with the three DsiRNAs targeting SETD8 (1 nM) is presented; DsiRNA #3 showed the most potent growth inhibitory effect. Statistical significance for each DsiRNA-transfected group was determined relative to the DsiNC-transfected control in each cell line using an unpaired two-tailed Student's t-test. *$p < 0.05$, **$p < 0.01$, ***$p < 0.001$, ****$p < 0.0001$, ns: not significant.

and ferroptosis resistance. In parallel, we found that SETD8 inhibition triggered a ferroptosis-like phenotype, characterized by accumulation of lipid peroxides. Transcriptomic profiling further revealed dysregulation of ferroptosis-related genes following SETD8 knockdown, including the upregulation of *EPAS1*, *ACSL4*, *NFE2L2*, and *BACH1*. ChIP-seq analysis revealed that *NFE2L2* exhibited increased H4K20me1 enrichment within its gene body, indicating that it may serve as a direct epigenetic target of SETD8. In contrast, the expression changes in the other ferroptosis-related genes are more likely attributable to indirect regulatory mechanisms or cell line-specific transcriptional responses. Collectively, these findings support a novel model in which SETD8 sustains the survival of OCCC cells by preserving redox homeostasis, identifying SETD8 as a previously unrecognized upstream epigenetic gatekeeper of ferroptosis[42,43].

Our findings raise important questions regarding the context-dependent nature of SETD8 function across different cancer types. Several factors may underlie this tumor-specific divergence. First, co-occurring genetic alterations, such as the frequent loss-of-function mutations in ARID1A and activating mutations in PIK3CA in OCCC, may reprogram the chromatin landscape in a manner that alters SETD8 target specificity and function[6,44]. Second, differences in the global chromatin state, including histone modification patterns and chromatin accessibility, can profoundly influence SETD8 recruitment and its ability to regulate downstream

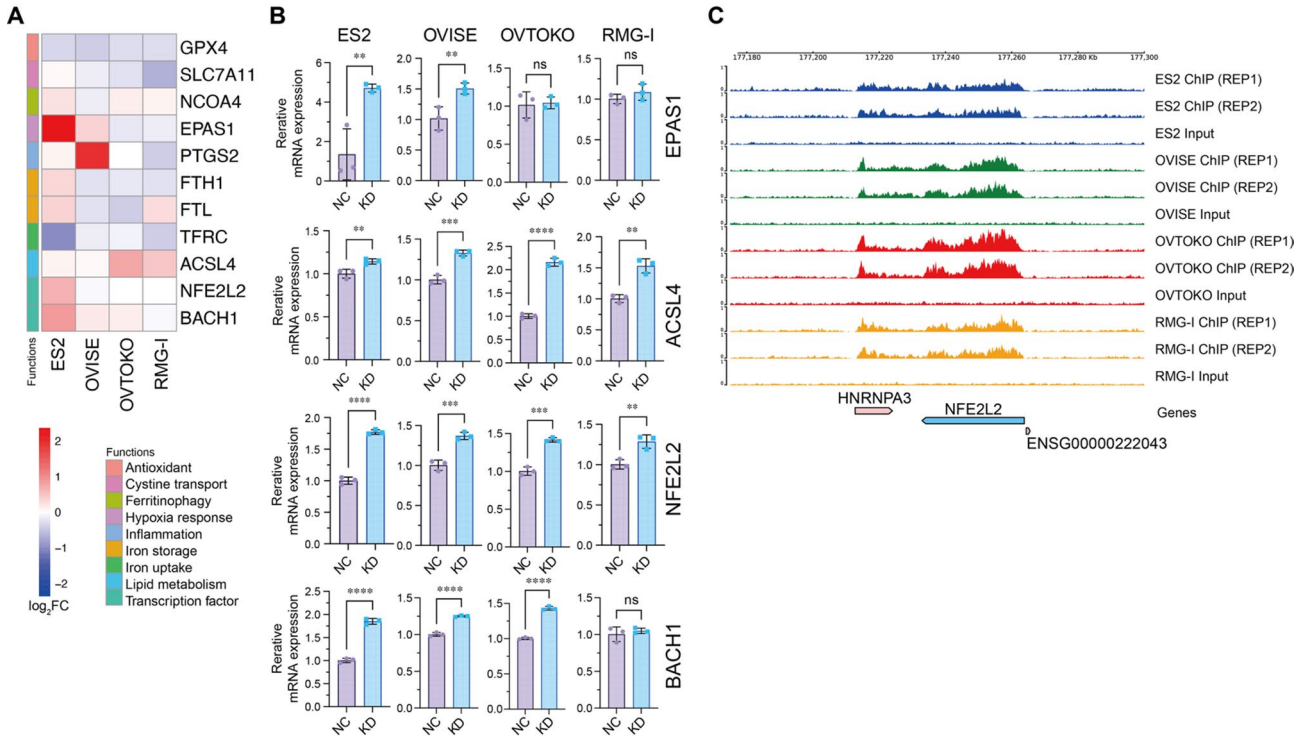

Fig. 5. SETD8 knockdown alters the expression of ferroptosis-related genes in OCCC. **A** Heatmap of RNA-seq–derived $\log_2$ fold-change values for ferroptosis-associated genes (*GPX4*, *SLC7A11*, *NCOA4*, *EPAS1*, *PTGS2*, *FTH1*, *FTL*, *TFRC*, *ACSL4*, *NFE2L2*, and *BACH1*) following SETD8 knockdown by DsiRNA #3 in four OCCC cell lines (ES2, OVISE, OVTOKO, and RMG-I), relative to the corresponding control. Genes are annotated by functional category. **B** Bar plots illustrating the upregulation of representative ferroptosis regulators (*EPAS1*, *ACSL4*, *NFE2L2*, *BACH1*) upon SETD8 knockdown, as determined by RT-qPCR. Expression levels were normalized to GAPDH. Data represent mean ± SD from three biological replicates ($n = 3$). Statistical significance for RNA-seq was assessed using edgeR (adjusted $p < 0.05$). RT-qPCR significance was determined using an unpaired two-tailed Student's t-test. $^{**}p < 0.01$; $^{***}p < 0.001$; $^{****}p < 0.0001$. NC: negative control; KD: knockdown. **C** Genome browser views of H4K20me1 enrichment at the *NFE2L2* gene locus.

gene expression[45,46]. Third, the availability or absence of cooperating transcriptional cofactors in OCCC versus other cancers, such as endometrial carcinoma, may modulate the transcriptional consequences of H4K20me1 deposition[47,48]. Lastly, cell type–specific metabolic demands and the baseline oxidative stress environment may sensitize OCCC cells to ferroptotic stress, thereby shaping the phenotypic outcomes of SETD8 depletion[49,50]. Together, these factors suggest that SETD8 does not operate as a universal oncogenic effector, but rather as a flexible chromatin regulator whose impact is dictated by the epigenetic and mutational context of each cancer type.

Further studies will be required to delineate the precise molecular mechanisms by which SETD8 orchestrates ferroptosis susceptibility and to determine the broader applicability of these findings across cancer types. One limitation of the present study is the lack of rescue experiments, such as the re-expression of SETD8 or pharmacological inhibition of downstream ferroptosis regulators. These approaches would be necessary to establish a direct causal relationship between SETD8 activity and ferroptosis susceptibility. Another important limitation is that, although SETD8 is primarily known as a histone H4K20 monomethyltransferase, we cannot exclude the possibility that the observed phenotypic effects are mediated through non-histone substrates or protein–protein interactions involving transcriptional regulatory complexes. In the absence of direct identification of downstream target genes regulated via H4K20me1, further studies will be essential to elucidate the transcriptional programs governed by SETD8 and to define their mechanistic contribution to OCCC pathogenesis.

An additional limitation of this study is the absence of in vivo validation using animal models, such as patient-derived xenografts (PDX). While in vivo studies are undoubtedly crucial for assessing the physiological and translational impact of SETD8 inhibition, the primary objective of the current study was to delineate the highly complex, cell-autonomous molecular mechanisms—specifically, the epigenetic regulation of RNA metabolism and its direct link to ferroptosis susceptibility via H4K20me1—in a controlled in vitro setting. Having established this foundational mechanistic framework, future in vivo studies will be essential to evaluate the systemic safety, pharmacokinetics, and therapeutic efficacy of targeting the SETD8 axis in OCCC.

In summary, based on our in vitro findings, we propose a model in which SETD8 sustains OCCC cell survival through dual roles: (1) epigenetically activating genes involved in RNA metabolism, and (2) preserving

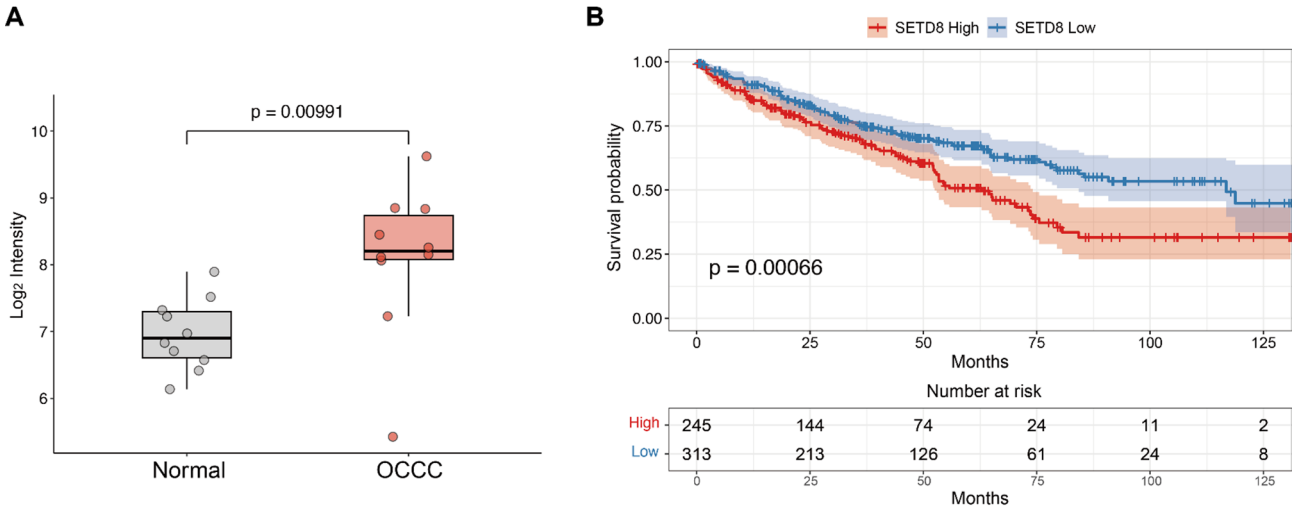

Fig. 6. **A***SETD8* is significantly upregulated in ovarian clear cell carcinoma (OCCC). mRNA expression levels of *SETD8* in normal ovarian surface epithelium (Normal; $n = 10$) and OCCC ($n = 10$) specimens were analyzed using the GSE29450 dataset. The y-axis represents the Log_2-transformed signal intensity. Each circle represents an individual sample. The box plot shows the median, quartiles, and range of the expression levels. A significant difference in *SETD8* expression was observed between the two groups ($p = 0.00991$, student's t-test). **B***SETD8* expression is significantly associated with poor overall survival in renal clear cell carcinoma (KIRC). Kaplan-Meier survival curves for patients in the TCGA-KIRC cohort stratified by *SETD8* mRNA expression levels. Patients were divided into high-expression (red line, $n = 245$) and low-expression (blue line, $n = 313$) groups based on the optimal expression threshold. The *p*-value ($p = 0.00066$) was calculated using the log-rank test. Shaded areas represent the 95% confidence intervals for each group. The number of patients at risk at each time interval (months) is provided in the risk table below the plot.

redox homeostasis by ensuring the proper processing and stability of transcripts encoding antioxidant defense components. The identification of this SETD8-RNA metabolism-ferroptosis axis provides a novel mechanistic framework for understanding the lineage-specific vulnerabilities of OCCC, distinct from its previously characterized functions in other gynecologic cancers.

Materials and methods

Clinical samples and compound sources

Fresh-frozen ovarian clear cell carcinoma (OCCC) specimens were obtained from patients treated at The University of Tokyo Hospital. Detailed clinical information for these cases is provided in Supplementary Table 2. The SETD8 inhibitor UNC0379 was purchased from MedChemExpress (Cat. No. HY-12335).

Cell lines and cell culture

The OCCC cell lines ES2, OVISE, OVTOKO, and RMG-I were used in this study. ES2 was obtained from ATCC (CRL-1978). OVISE (JCRB1043), OVTOKO (JCRB1048), and RMG-I (JCRB0172) were acquired from the Japanese Collection of Research Bioresources (JCRB) Cell Bank. Cell line authentication was confirmed by short tandem repeat (STR) profiling[51]. The absence of mycoplasma contamination was routinely verified using the e-Myco Mycoplasma PCR Detection Kit (iNtRON Biotechnology, Inc., Cat. No. 25235), following the manufacturer's instructions. Cells were cultured according to the supplier's guidelines: ES2 in McCoy's 5 A medium (Gibco, 16600082); OVISE and OVTOKO in RPMI-1640 medium (FUJIFILM-Wako, 189–02025); and RMG-I in Ham's F-12 medium (FUJIFILM-Wako, 087-08335). All media were supplemented with 10% fetal bovine serum (FBS; Gibco, 10270106), 100 U/mL penicillin, and 100 µg/mL streptomycin (Gibco, 15240-062). Cells were maintained at 37 °C in a humidified incubator with 5% CO_2.

DsiRNA transfection

Three distinct DsiRNAs targeting *SETD8* were obtained as part of the TriFECTa RNAi Kit (Integrated DNA Technologies, IDT). A non-targeting DsiRNA was included as a negative control to assess potential non-specific effects. The sequences of all RNA duplexes are listed in Supplementary Table 3. Transfections were performed using a final DsiRNA concentration of 1 nM. Reverse transfection was carried out using Lipofectamine RNAiMAX (Invitrogen, 13778150), according to the manufacturer's protocol. Briefly, transfection complexes were first prepared in Opti-MEM reduced serum medium (Gibco, 31985070) by mixing DsiRNA and Lipofectamine RNAiMAX, followed by incubation at 25℃ for 20 min. These complexes were then added directly to wells before seeding cells in antibiotic-free medium at a density corresponding to 40–60% confluency. After a 4-hour incubation, an equal volume of complete growth medium was added to each well.

Quantitative real-time PCR (RT-qPCR)

Total RNA was extracted from cultured cells using the RNeasy Mini Kit (Qiagen, Inc.) following the manufacturer's instructions. First-strand complementary DNA (cDNA) was synthesized from total RNA using the ReverTra Ace qPCR RT Master Mix with gDNA Remover (Toyobo Co., Ltd.). RT-qPCR was conducted using the One Step SYBR PrimeScript RT-PCR Kit (Takara Bio, Inc.) on a QuantStudio Real-Time PCR System (Thermo Fisher Scientific, Inc.). Thermal cycling conditions were as follows: initial denaturation at 98 °C for 2 min, followed by 45 cycles of 98 °C for 10 s, 62 °C for 10 s, and 68 °C for 30 s. *ACTB* or *GAPDH* was used as an internal reference gene. Relative gene expression levels were calculated using the $2^{\wedge-\Delta\Delta Cq}$ method. Primer sequences used in the study are listed in Supplementary Table 3.

Western blotting

Cells were lysed directly in CelLytic M Cell Lysis Reagent (Sigma-Aldrich, Cat. No. C2978), supplemented with protease and phosphatase inhibitors (Roche, Cat. No. 04693159001; SERVA, Cat. No. 39050). Whole-cell lysates were homogenized by passing them through a 25-gauge needle ten times and subsequently centrifuged to remove insoluble debris. Protein concentrations were determined using the Pierce 660 nm Protein Assay Reagent (Thermo Fisher Scientific, Cat. No. 22660), following the manufacturer's protocol. Equal amounts of total protein were mixed with Lane Marker Reducing Sample Buffer (Thermo Fisher Scientific, Cat. No. 39000), denatured by heating at 95 °C for 5 min, and separated by SDS-PAGE using precast polyacrylamide gels (Bio-Rad, Cat. No. 456–9034). Proteins were then transferred onto nitrocellulose membranes (GE Healthcare, Cat. No. 10600012) via standard wet transfer. Membranes were blocked with 5% skim milk in TBS-T (FUJIFILM Wako, Cat. No. 190-12865) for 1 h at 25 °C and incubated overnight at 4 °C with the following primary antibodies: Mono-Methyl-Histone H4 (Lys20) Antibody (Cell Signaling Technology, Cat. No. 9724), SET8 (C18B7) Antibody (Cell Signaling Technology, Cat. No. 2996), and β-Actin (Sigma-Aldrich, Cat. No. A2228). After washing, membranes were incubated with HRP-conjugated secondary antibodies: anti-mouse IgG (GE Healthcare, Cat. No. NA931; 1:5000) and anti-rabbit IgG (GE Healthcare, Cat. No. NA934; 1:5000). Signals were detected using the ECL Prime Western Blotting Detection Reagent (GE Healthcare, Cat. No. RPN2236) and imaged using the ImageQuant LAS 4000 system (GE Healthcare). Densitometric quantification of protein bands was performed using ImageJ software.

Cell proliferation assays

1. **RNA interference-based assays**

Cells were seeded into 96-well plates at a density of 1,000 to 3,000 cells per well and transfected with DsiRNAs using Lipofectamine RNAiMAX, as described in the previous section.

2. **Chemical inhibitor-based assays**.

The same cell lines were seeded at a density of 2,000 cells per well in 96-well plates. After 24 h of incubation, the cells were treated with the specified concentrations of SETD8 inhibitors and maintained in culture for an additional 72 h.

At the designated time points, 10 µL of Cell Counting Kit-8 reagent (Dojindo, 341–08001) was added to each well. Following a 2-hour incubation at 37℃, absorbance at 450 nm was measured using a Multiskan FC microplate reader (Thermo Fisher Scientific) to assess cell viability.

Colony formation assays

Cells were seeded into 6-well plates at a density of 1,000 to 3,000 cells per well and allowed to adhere overnight. The following day, cells were treated with the SETD8 inhibitor UNC0379 at the specified final concentrations. To achieve the desired concentration, 500 µL of compound solution, prepared at 4× the final concentration in complete growth medium, was added to 1.5 mL of the existing medium in each well, resulting in a total volume of 2 mL. Control wells received 500 µL of vehicle (DMSO) diluted in the same manner. Cells were incubated for 10 to 14 days, with the medium replaced every 3 to 4 days. At the endpoint, colonies were fixed with 1% formaldehyde and stained with a solution containing 0.05% crystal violet and 1% methanol for 20 min at 25 °C. Wells were subsequently washed with distilled water and air-dried.

Lipid peroxidation analysis by C11-BODIPY 581/591 imaging

To assess lipid reactive oxygen species (lipid ROS) production upon SETD8 inhibition, lipid peroxidation imaging was performed using the fluorescent probe C11-BODIPY 581/591 (Thermo Fisher Scientific, D3861). Two experimental approaches were used: genetic knockdown of SETD8 through DsiRNA and pharmacological inhibition with UNC0379. Four cell lines were used: ES2, OVISE, OVTOKO, and RMG-I. Each cell line was maintained in its respective culture medium supplemented with 10% fetal bovine serum (FBS) and 1% penicillin-streptomycin, following standard protocols. Cells were seeded into 96-well black clear-bottom microplates (Agilent, Cat. No. 204626-100) at densities ranging from 3,000 to 7,500 cells per well, depending on the proliferation rate of each cell line.

Reverse transfection was performed using the TriFECTa RNAi Kit with DsiRNAs targeting SETD8 or a negative control DsiRNA, as described in the above section. In each well, 20 µL of Opti-MEM containing 0.1 µL of 1 µM DsiRNA was mixed with 0.2 µL of Lipofectamine RNAiMAX, incubated at 25℃ for 20 min, and then combined with 80 µL of cell suspension. After 4 h, an additional 100 µL of complete medium was added. Cells were incubated for 72 h at 37 °C with 5% CO_2. For chemical inhibition, UNC0379 was added the day after

seeding at final concentrations of 1, 5, and 10 μM. DMSO was used as a vehicle control. Cells were incubated with the compound for 48 h under standard conditions. After either 72 h of DsiRNA treatment or 48 h of inhibitor treatment, cells were incubated with 10 μM C11-BODIPY 581/591, freshly diluted in complete medium, for 30 min at 37 °C. Cells were washed three times with PBS, and 280 μL of PBS was added per well for imaging. Imaging was performed using a BioTek Cytation5 Cell Imaging Multi-Mode Reader (Agilent) equipped with a 4× objective lens. The following fluorescence channels were utilized: GFP filter (EX 469/35 nm, EM 525/39 nm) to detect the oxidized lipid signal (green) and Texas Red filter (EX 586/15 nm, EM 647/57 nm) to detect the unoxidized lipid signal (red). Image acquisition and analysis were conducted using Gen5 Software (Agilent). To determine the threshold for counting GFP(+) and Texas Red(+) cells, the Line Profile tool was used to evaluate representative regions across multiple images. This tool extracted fluorescence intensity values along defined linear paths, and the suggested "25% = value" output was adopted as a reference point to establish an initial threshold. The same threshold was uniformly applied across samples to ensure consistency. Lipid peroxidation was quantified using the following ratio: GFP(+) / Texas Red(+) × 100. All conditions were tested in three technical replicates (triplicates).

RNA sequencing (RNA-seq)

ES2, OVISE, OVTOKO, and RMG-I cells were transfected with DsiRNA (hs.Ri.SETD8.13.3) as described in the previous section. After 72 h of incubation post-transfection, total RNA was isolated for library preparation. Total RNA was extracted using QIAzol Lysis Reagent and the RNeasy Plus Mini Kit (Qiagen, Cat. No. 73404), according to the manufacturer's instructions. RNA quantity and purity were assessed using a NanoDrop spectrophotometer (Thermo Fisher Scientific), and RNA integrity was evaluated using an Agilent TapeStation system (Agilent Technologies). Complementary DNA (cDNA) synthesis was performed using the PrimeScript RT Reagent Kit with gDNA Eraser (TaKaRa Bio, Cat. No. RR037A) following the manufacturer's protocol. RNA-seq libraries were prepared using the NEBNext Ultra II Directional RNA Library Prep Kit for Illumina (New England Biolabs), following the manufacturer's recommendations for poly(A)-enriched, strand-specific transcriptome analysis. Libraries were validated for quality and fragment size using the Agilent TapeStation system. Libraries were sequenced on the Illumina NovaSeq 6000 with 50 bp paired-end reads to achieve an average depth of 50 million reads per sample.

Chromatin immunoprecipitation and sequencing (ChIP-seq)

ChIP-seq experiments were performed in a stepwise manner, following established protocols with minor modifications[52], as described below: cultured cells (from 1 to 2×15 cm dishes) were harvested and washed once with PBS. Cells were crosslinked with 1% formaldehyde (Sigma-Aldrich, molecular biology grade) in pre-warmed PBS for 10 min at 25℃ with gentle rotation. Crosslinking was quenched by adding 1/20 volume of 2.5 M glycine followed by shaking for 5 min at 25℃. Cells were pelleted by centrifugation at 500 × *g* for 5 min and washed once with PBS. After a second centrifugation, the supernatant was removed, and the pellet was snap-frozen in liquid nitrogen and stored at − 80℃. Frozen pellets were resuspended in Lysis Buffer (50 mM HEPES [pH 7.5], 140 mM NaCl, 1 mM EDTA, 10% glycerol, 0.5% Igepal CA-630, 0.25% Triton X-100 with protease inhibitor cocktail), incubated on a rotator at 4 °C for 10 min, and pelleted. The pellet was then resuspended in Wash Buffer (10 mM Tris-HCl [pH 8.0], 200 mM NaCl, 1 mM EDTA, 0.5 mM EGTA) and incubated again at 4 °C for 10 min. After centrifugation, the pellet was resuspended in Sonication Buffer (10 mM Tris-HCl [pH 8.0], 1 mM EDTA, 0.1% SDS) at 10× the pellet volume and transferred to sonication tubes. Chromatin was sheared using a Bioruptor II (15 cycles of 30 s ON/30 s OFF at high power). Fragmentation was assessed by Agilent TapeStation. Chromatin was diluted with 10× ChIP Dilution Buffer (10% Triton X-100, 1 M NaCl, 1% sodium deoxycholate, 5% N-lauroylsarcosine, 5 mM EGTA), clarified by centrifugation, and the supernatant was collected. A small aliquot of sonicated chromatin (10 μL) was incubated with ChIP Elution Buffer (CST), 5 M NaCl, and 20 mg/mL proteinase K (NEB) at 65 °C for 2 h with shaking. DNA was purified using the PCR purification kit (Qiagen) and quantified using Qubit3 and Agilent TapeStation. Chromatin (5 μg) was incubated overnight at 4 °C with 1 μL of anti-Histone H4 (mono methyl K20) antibody (Abcam, 9051, Lot # GR3344957-1, 1 mg/mL) in a final volume of 250 μL. Samples were incubated with 2.5 μL FG Beads HM Protein G (Tamagawa Seiki) for 1 h at 4 °C. Beads were collected using DynaMag-2 (Invitrogen) and washed three times with RIPA Buffer (50 mM HEPES [pH 7.5], 500 mM LiCl, 1 mM EDTA, 1% NP-40, 0.7% sodium deoxycholate) and once with TE buffer containing 50 mM NaCl. Beads were resuspended in 94 μL of ChIP Elution Buffer, incubated at 65 °C for 30 min with shaking, and the supernatant was transferred to a new tube. Proteinase K (2 μL, 20 mg/mL) and NaCl (4 μL, 5 M) were added, and samples were incubated at 65 °C for at least 2 h (up to overnight). DNA was purified using a PCR purification kit (Qiagen) and eluted in 50 μL of elution buffer. Libraries were prepared using the QIAseq Ultralow Input Library Kit (Qiagen) following the manufacturer's instructions. Typically, 10 PCR cycles were used for 10 ng of DNA fragment. Library quality was assessed using Agilent TapeStation. ChIP-seq libraries were sequenced on the Illumina NovaSeq 6000 platform using paired-end 50-bp reads at a depth of approximately 30–50 million reads per sample.

RNA-seq data processing and analysis

Raw RNA-seq data were processed using the nf-core/rnaseq pipeline (version 3.6), which provides a standardized workflow for quality control, read trimming, alignment, quantification, and downstream analysis of RNA-seq data[53]. Adapter sequences and low-quality bases were trimmed using Trim Galore (version 0.6.6), a wrapper tool that integrates Cutadapt and FastQC for quality filtering. Sequencing reads were then aligned to the human reference genome (hg38) using STAR (version 2.7.6a). Gene-level transcript quantification was performed using Salmon (version 1.5.2). Gene-level counts were aggregated using tximport, and differential gene expression analysis was performed using edgeR (version 3.42.4) within the R statistical environment. Genes with an

adjusted p-value < 0.05 were considered significantly differentially expressed. Unless otherwise stated, all tools were executed with default parameters.

ChIP-seq data processing and analysis

Raw ChIP-seq data were processed using the nf-core/chipseq pipeline (version 1.2.2), which performs standardized quality control and preprocessing of next-generation sequencing data[53]. Briefly, sequencing reads were aligned to the human reference genome (hg38) using Bowtie2 (version 2.2.9) with the --local alignment option to improve sensitivity at read ends. PCR duplicates were identified and removed using Samtools (version 1.3.1) to minimize redundancy and bias in downstream analyses. Peak calling to identify enriched regions (ERs) was performed using MACS3, employing the corresponding input control samples to model the background signal. Unless otherwise stated, default parameters were used for all tools. Peak annotation and further analysis were performed using the ChIPpeakAnno package (version 3.34.1).

To assess the global similarity of ChIP-seq profiles across samples, we performed hierarchical clustering and sample-to-sample distance analysis using the DESeq2 package. A consensus peak set was generated by merging all peaks identified by MACS3 across the samples using bedtools. This non-redundant set of genomic intervals was used to construct a count matrix, in which the number of sequencing reads overlapping each region was quantified for each sample using the featureCounts function. The count data were normalized using variance-stabilizing transformation (VST) implemented in DESeq2, which stabilizes the variance across a wide range of mean values. Pairwise distances between samples were computed based on Euclidean distance applied to the VST-transformed matrix. The resulting distance matrix was visualized as a heatmap using the pheatmap package, with hierarchical clustering performed to reveal global similarities and clustering patterns among the ChIP-seq samples.

Analysis of public microarray data

To investigate the clinical expression levels of *SETD8* in OCCC, we utilized the public microarray dataset GSE29450 retrieved from the Gene Expression Omnibus (GEO) database[40]. This dataset includes gene expression profiles from 10 micro-dissected OCCC tumors and 10 normal ovarian surface epithelium (OSE) samples. For this analysis, Log2-transformed intensity values for the representative probe set of *SETD8* were extracted. Statistical significance between the normal and OCCC groups was determined using a student's t-test.

Survival analysis using public datasets

To evaluate the clinical impact of SETD8 in clear cell lineage tumors, we retrieved transcriptomic and clinical follow-up data from the TCGA-KIRC (Kidney Renal Clear Cell Carcinoma) cohort via cBioPortal[54]. A total of 558 primary tumor samples with available survival data were included in the analysis. Overall survival (OS) was defined as the time from diagnosis to death or last follow-up. Patients were categorized into *SETD8*-high and *SETD8*-low groups based on mRNA expression levels. Survival probabilities were estimated using the Kaplan-Meier method, and differences between the two groups were evaluated using the log-rank test. All statistical analyses and visualizations were performed using R software with the survival and survminer packages.

Statistical analysis

Unless otherwise indicated, all statistical analyses were performed using GraphPad Prism version 10.1.2.

Data availability

Newly generated data

The raw FastQ files from ChIP-seq and RNA-seq generated during this study have been deposited in the DNA Data Bank of Japan (DDBJ) under the accession number DRA020623. The processed dataset used for this study is publicly available via Figshare at the following DOI:

https://doi.org/10.6084/m9.figshare.28852388. This dataset contains bigWig files derived from ChIP-seq experiments conducted to profile genome-wide H4K20me1 occupancy, as well as gene-level raw read count matrices from RNA-seq experiments performed on the same OCCC cell lines transfected with either SETD8-targeting or control DsiRNAs.

Public OC dataset

The sequencing data (RNA-seq and ChIP-seq) for endometrial cancer cell lines used for comparative analysis in this study are available in the BioProject database under accession number PRJDB12770.

(https://ddbj.nig.ac.jp/resource/bioproject/PRJDB12770). These data are also linked to the Sequence Read Archive (SRA) study DRP009168.

The microarray dataset for ovarian clear cell carcinoma ($n = 10$) and normal ovarian surface epithelium ($n = 10$) analyzed for clinical validation was retrieved from the NCBI Gene Expression Omnibus (GEO) under the accession number GSE29450 (https://www.ncbi.nlm.nih.gov/geo/query/acc.cgi? acc=GSE29450).

TCGA-KIRC data

The transcriptomic and clinical datasets for the Kidney Renal Clear Cell Carcinoma (TCGA-KIRC) cohort are available through the Genomic Data Commons (GDC) portal (https://portal.gdc.cancer.gov/projects/TCGA-KIRC) and were accessed via cBioPortal (https://www.cbioportal.org/).

Received: 2 January 2026; Accepted: 9 April 2026
Published online: 15 April 2026

References

1. Kurman, R. J. & Shih Ie, M. The origin and pathogenesis of epithelial ovarian cancer: a proposed unifying theory. *Am. J. Surg. Pathol.* **34**, 433–443 (2010).
2. Medina-Perucha, L. et al. Endometriosis prevalence and incidence trends in a large population-based study in Catalonia (Spain) from 2009 to 2018. *Womens Health (Lond)*. **18**, 17455057221130566 (2022).
3. Shen, D. Y., Li, J., Hu, P., Qi, C. & Yang, H. Global, regional, and national prevalence and disability-adjusted life-years for endometriosis in 204 countries and territories, 1990–2019: Findings from a global burden of disease study. *Eur. J. Obstet. Gynecol. Reprod. Biol. X.* **25**, 100363 (2025).
4. Anglesio, M. et al. (ed, S.) Clear cell carcinoma of the ovary: a report from the first Ovarian Clear Cell Symposium, June 24th, 2010. *Gynecol. Oncol.* **121**407–415 (2011).
5. Kuo, K. T. et al. Frequent activating mutations of PIK3CA in ovarian clear cell carcinoma. *Am. J. Pathol.* **174**, 1597–1601 (2009).
6. Wiegand, K. C. et al. ARID1A mutations in endometriosis-associated ovarian carcinomas. *N Engl. J. Med.* **363**, 1532–1543 (2010).
7. Sia, T. Y. et al. Treatment of ovarian clear cell carcinoma with immune checkpoint blockade: a case series. *Int. J. Gynecol. Cancer*. **32**, 1017–1024 (2022).
8. Tamura, R., Yoshihara, K. & Enomoto, T. Therapeutic Strategies Focused on Cancer-Associated Hypercoagulation for Ovarian Clear Cell Carcinoma. *Cancers (Basel)* 14 (2022).
9. Shi, X. et al. Modulation of p53 function by SET8-mediated methylation at lysine 382. *Mol. Cell.* **27**, 636–646 (2007).
10. Takawa, M. et al. Histone lysine methyltransferase SETD8 promotes carcinogenesis by deregulating PCNA expression. *Cancer Res.* **72**, 3217–3227 (2012).
11. Tardat, M. et al. The histone H4 Lys 20 methyltransferase PR-Set7 regulates replication origins in mammalian cells. *Nat. Cell. Biol.* **12**, 1086–1093 (2010).
12. Zhang, X. et al. Histone methyltransferase SET8 is regulated by miR-192/215 and induces oncogene-induced senescence via p53-dependent DNA damage in human gastric carcinoma cells. *Cell. Death Dis.* **11**, 937 (2020).
13. Veschi, V. et al. Epigenetic siRNA and Chemical Screens Identify SETD8 Inhibition as a Therapeutic Strategy for p53 Activation in High-Risk Neuroblastoma. *Cancer Cell.* **31**, 50–63 (2017).
14. Kukita, A. et al. The Histone Methyltransferase SETD8 Regulates the Expression of Tumor Suppressor Genes via H4K20 Methylation and the p53 Signaling Pathway in Endometrial Cancer Cells. *Cancers (Basel)* 14 (2022).
15. Zou, Y. et al. A GPX4-dependent cancer cell state underlies the clear-cell morphology and confers sensitivity to ferroptosis. *Nat. Commun.* **10**, 1617 (2019).
16. Lamperis, S. M. et al. CRISPR screen reveals a simultaneous targeted mechanism to reduce cancer cell selenium and increase lipid oxidation to induce ferroptosis. *Proc. Natl. Acad. Sci. U S A*. **122**, e2502876122 (2025).
17. Doll, S. et al. ACSL4 dictates ferroptosis sensitivity by shaping cellular lipid composition. *Nat. Chem. Biol.* **13**, 91–98 (2017).
18. Jiang, L. et al. Ferroptosis as a p53-mediated activity during tumour suppression. *Nature* **520**, 57–62 (2015).
19. Zhou, Q. et al. Ferroptosis in cancer: From molecular mechanisms to therapeutic strategies. *Signal. Transduct. Target. Ther.* **9**, 55 (2024).
20. Yang, W. S. & Stockwell, B. R. Ferroptosis: Death by Lipid Peroxidation. *Trends Cell. Biol.* **26**, 165–176 (2016).
21. Lin, W. et al. SLC7A11/xCT in cancer: biological functions and therapeutic implications. *Am. J. Cancer Res.* **10**, 3106–3126 (2020).
22. Anglesio, M. S. et al. Type-specific cell line models for type-specific ovarian cancer research. *PLoS One*. **8**, e72162 (2013).
23. Arafeh, R., Shibue, T., Dempster, J. M., Hahn, W. C. & Vazquez, F. The present and future of the Cancer Dependency Map. *Nat. Rev. Cancer*. **25**, 59–73 (2025).
24. Ghandi, M. et al. Next-generation characterization of the Cancer Cell Line Encyclopedia. *Nature* **569**, 503–508 (2019).
25. Kim, D. H. et al. Synthetic dsRNA Dicer substrates enhance RNAi potency and efficacy. *Nat. Biotechnol.* **23**, 222–226 (2005).
26. Pichu, S. et al. Knockdown of Ki-67 by dicer-substrate small interfering RNA sensitizes bladder cancer cells to curcumin-induced tumor inhibition. *PLoS One*. **7**, e48567 (2012).
27. Bursac, S., Prodan, Y., Pullen, N., Bartek, J. & Volarevic, S. Dysregulated Ribosome Biogenesis Reveals Therapeutic Liabilities in Cancer. *Trends Cancer*. **7**, 57–76 (2021).
28. Jaiswal, P. K., Koul, S., Palanisamy, N. & Koul, H. K. Eukaryotic Translation Initiation Factor 4 Gamma 1 (EIF4G1): a target for cancer therapeutic intervention? *Cancer Cell. Int.* **19**, 224 (2019).
29. Jia, R. & Zheng, Z. M. Oncogenic SRSF3 in health and diseases. *Int. J. Biol. Sci.* **19**, 3057–3076 (2023).
30. Liu, E. Y., Cali, C. P. & Lee, E. B. RNA metabolism in neurodegenerative disease. *Dis. Model. Mech.* **10**, 509–518 (2017).
31. Lu, Y. et al. Heterogeneous nuclear ribonucleoprotein A/B: an emerging group of cancer biomarkers and therapeutic targets. *Cell. Death Discov.* **8**, 337 (2022).
32. Pelletier, J., Thomas, G. & Volarevic, S. Ribosome biogenesis in cancer: new players and therapeutic avenues. *Nat. Rev. Cancer*. **18**, 51–63 (2018).
33. Ma, A. et al. Discovery of a selective, substrate-competitive inhibitor of the lysine methyltransferase SETD8. *J. Med. Chem.* **57**, 6822–6833 (2014).
34. Ma, A. et al. Structure-activity relationship studies of SETD8 inhibitors. *Medchemcomm* **5**, 1892–1898 (2014).
35. Veschi, V. et al. C1Q(+) TPP1(+) macrophages promote colon cancer progression through SETD8-driven p53 methylation. *Mol. Cancer*. **24**, 102 (2025).
36. Yang, X., Guan, Y., Bayliss, G., Zhao, T. C. & Zhuang, S. SET8 inhibition preserves PTEN to attenuate kidney cell apoptosis in cisplatin nephrotoxicity. *Cell. Death Dis.* **16**, 226 (2025).
37. Jiang, X., Stockwell, B. R. & Conrad, M. Ferroptosis: mechanisms, biology and role in disease. *Nat. Rev. Mol. Cell. Biol.* **22**, 266–282 (2021).
38. Stockwell, B. R. et al. Ferroptosis: A Regulated Cell Death Nexus Linking Metabolism, Redox Biology, and Disease. *Cell* **171**, 273–285 (2017).
39. Dai, C. et al. Transcription factors in ferroptotic cell death. *Cancer Gene Ther.* **27**, 645–656 (2020).
40. Stany, M. P. et al. Identification of novel therapeutic targets in microdissected clear cell ovarian cancers. *PLoS One*. **6**, e21121 (2011).
41. Murga, M. et al. SETD8 inhibition targets cancer cells with increased rates of ribosome biogenesis. *Cell. Death Dis.* **15**, 694 (2024).
42. Long, G. et al. Ferroptosis-related alternative splicing signatures as potential biomarkers for predicting prognosis and therapy response in gastric cancer. *Heliyon* **10**, e34381 (2024).
43. Luo, S. H. et al. The BRD4-SRPK2-SRSF2 signal modulates the splicing efficiency of ACSL3 pre-mRNA and influences erastin-induced ferroptosis in osteosarcoma cells. *Cell. Death Dis.* **14**, 760 (2023).
44. Bitler, B. G. et al. ARID1A-mutated ovarian cancers depend on HDAC6 activity. *Nat. Cell. Biol.* **19**, 962–973 (2017).
45. Girish, T. S., McGinty, R. K. & Tan, S. Multivalent Interactions by the Set8 Histone Methyltransferase With Its Nucleosome Substrate. *J. Mol. Biol.* **428**, 1531–1543 (2016).
46. Zhou, V. W., Goren, A. & Bernstein, B. E. Charting histone modifications and the functional organization of mammalian genomes. *Nat. Rev. Genet.* **12**, 7–18 (2011).
47. Buenrostro, J. D. et al. Single-cell chromatin accessibility reveals principles of regulatory variation. *Nature* **523**, 486–490 (2015).
48. Marand, A. P. et al. The genetic architecture of cell type-specific cis regulation in maize. *Science* **388**, eads6601 (2025).
49. Hangauer, M. J. et al. Drug-tolerant persister cancer cells are vulnerable to GPX4 inhibition. *Nature* **551**, 247–250 (2017).

50. Tsoi, J. et al. Multi-stage Differentiation Defines Melanoma Subtypes with Differential Vulnerability to Drug-Induced Iron-Dependent Oxidative Stress. *Cancer Cell.* **33**, 890–904e895 (2018).
51. Dozen, A. et al. Tumor Suppressive Role of the PRELP Gene in Ovarian Clear Cell Carcinoma. *J Pers. Med* **12** (2022).
52. Kaneko, S. et al. Mechanism of ERBB2 gene overexpression by the formation of super-enhancer with genomic structural abnormalities in lung adenocarcinoma without clinically actionable genetic alterations. *Mol. Cancer.* **23**, 126 (2024).
53. Ewels, P. A. et al. The nf-core framework for community-curated bioinformatics pipelines. *Nat. Biotechnol.* **38**, 276–278 (2020).
54. Cancer Genome Atlas Research, N. Comprehensive molecular characterization of clear cell renal cell carcinoma. *Nature* **499**, 43–49 (2013).

Acknowledgements
We thank Dr. Shinkai for his valuable assistance with data deposition and for ensuring the integrity and accessibility of the datasets associated with this study. The results shown here are in part based upon data generated by the TCGA Research Network: https://www.cancer.gov/tcga.

Author contributions
E.S., S.K., and K.S. conceived and designed the study. E.S., S.K., N.I., R.H., Y.J., N.T., and A.T. performed the experiments and data collection. E.S., S.K., K.S., and N.I. conducted the bioinformatics analysis and interpretation. K.S., Y.J., N.T., and A.T. provided clinical insights into the study. K.A., M.K., T.I., K.O., Y.O., Y.H., and R.Ha. supervised the project. S.K. drafted the manuscript with input from all authors. All authors reviewed and approved the final manuscript.

Funding
This work was supported by the JSPS Grant-in-Aid for Scientific Research (Grant Number JP24K03039), the Takeda Science Foundation and the Research Grant of the Princess Takamatsu Cancer Research Fund (19-25108) to S.K.; and by the National Cancer Center Research and Development Fund (2023-A-04) and the Cabinet Office BRIDGE (programs for bridging the gap between R&D and the ideal society (Society 5.0) and generating economic and social value) to R.H.

Declarations

Competing interests
The authors declare no competing interests.

Ethics declarations
This study was conducted in accordance with the ethical guidelines for medical and health research involving human subjects and adhered to the principles of the Declaration of Helsinki. Written informed consent was obtained from all participating patients prior to study enrollment. The study protocol was approved by the Institutional Review Board of the National Cancer Center, Japan (approval number: 2016 – 496), and by the Human Genome and Gene Analysis Research Ethics Committee of the University of Tokyo (approval number: G0683-28).

Additional information
Supplementary Information The online version contains supplementary material available at https://doi.org/10.1038/s41598-026-48676-z.

Correspondence and requests for materials should be addressed to S.K. or K.S.